LARGE EDDY SIMULATION APPLIED ON VORTEX INDUCED VIBRATION PROBLEMS

J. B. V. Wanderley, Ph.D.
Ocean Engineering Program, COPPE, UFRJ, Technology Center,
Building C, Room 203, Rio de Janeiro, RJ, CEP.: 21945-970, Brazil
E: juanw@peno.coppe.ufrj.br

C. A. Levi, Ph.D.
Ocean Engineering Program, COPPE, UFRJ, Technology Center,
Building C, Room 203, Rio de Janeiro, RJ, CEP.: 21945-970, Brazil
E: levi@peno.coppe.ufrj.br

Abstract. The Vortex-induced vibration on a circular cylinder is investigated by the numerical solution of the unsteady Navier-Stokes equations and results are compared with experimental measurements obtained by different authors. The Beam and Warming implicit factored scheme is used to solve the governing equations and Large Eddy Simulation is used together with the Smagorinsky subgrid-scale model (SGS) to simulate the turbulent flow in the wake of the cylinder. The cylinder is laterally supported by a spring and a damper and is free to oscillate in the transversal direction in an initially uniform flow for the first flow speed investigated. For the subsequent speeds, the final condition obtained for the previous speed is used as initial condition to reproduce the actual experimental set up. In that case, the measurements are done by progressive increments of the flow speed retaining the fluid memory effect. The complexity and high sensitivity of the flow phenomenon at this configuration requires a very accurate and robust numerical model. Most of the known algorithms failed to duplicate the available experimental measurements. The proposed numerical solution was able to provide a good picture of the real physics of the phenomenon showing the Kármán vortex street effects on the lift and drag coefficients. The numerical results for the transversal oscillation amplitude are compared to experimental data showing a fairly precise agreement at the difficult to simulate regime of the lock-in phenomenon.

Keywords. *Navier – Stokes, Computational Fluid Dynamics, Vortex Induced Vibration, Large Eddy Simulatio*

1. Introdução

Vortex-induced vibration (VIV) is a direct consequence of lift and drag oscillations due to the vortex shedding. When the frequency of vortex shedding coincides with the structural natural frequency, the VIV can occur with high dangerous amplitudes that may cause failure of the excited structure. For a fixed body, the vortex shedding frequency is a function of the Reynolds number. For a moving cylinder, Bearman (2000), the fluid interacts strongly with the cylinder motion and the vortex shedding frequency is captured by the body frequency over a wider range of flow speed. This is known as lock-in and the extent of this range depends on the structural damping and mass ratio of the cylinder.

The motivation for the present work is to simulate numerically the experimental work done by Khalak and Williamson (1996) measuring the oscillating cylinder amplitude. In their work, the amplitude of the cylinder oscillation was measured imposing a progressive increment of the reduced velocity with the Reynolds number increasing from 2000 up to 12000. In this range of Reynolds number, the boundary layer on the body is still laminar, but the wake is completely turbulent. In the present work, the Beam and Warming (1978) implicit factored scheme is used to solve the unsteady Navier-Stokes equations and Large Eddy Simulation is used together with the Smagorinsky (1963) subgrid-scale model (SGS) to simulate the turbulent flow of the wake. Since vortex stretching strongly dominates the turbulent production, the 2D simulation seems to be inadequate for capturing the important scales of turbulent physics. However, 3D computation is very expensive and time consuming especially in the study of the VIV phenomenon. In 2D flow there is no vortex stretching so that the transfer of energy mentioned above is not as efficient as in the 3D case. Nevertheless, 2D computation is able to produce fairly good results and at the same time it keeps its efficiency regarding the time of computation, Flatschart *et al* (2000). The numerical solution was able to capture the real physics of the phenomenon showing the Kármán vortex street effects on the lift and drag coefficients. The numerical results for the transversal oscillation amplitude compares well to the experimental data showing a fairly good qualitative and quite precise agreement of the lock-in phenomenon, where other numerical simulations have failed.

2. Mathematical Formulation

In Large Eddy Simulation (LES), the large-scale turbulence structure is computed directly in the numerical simulation and the effects of the small scale structure are modeled using a subgrid-scale (SGS) model. The governing equations are obtained by filtering the Navier-Stokes equations by a local volume averaging. From Bui (2000), the filtered continuity and momentum equations are shown below.

$$\frac{\partial \bar{\rho}}{\partial t} + \frac{\partial \bar{\rho}\tilde{u}}{\partial x} + \frac{\partial \bar{\rho}\tilde{v}}{\partial y} + \frac{\partial \bar{\rho}\tilde{w}}{\partial z} = 0 \tag{1}$$

$$\frac{\partial \bar{\rho}\tilde{u}}{\partial t}+\frac{\partial\left(\bar{\rho}\tilde{u}^2+\bar{p}\right)}{\partial x}+\frac{\partial \bar{\rho}\tilde{u}\tilde{v}}{\partial y}+\frac{\partial \bar{\rho}\tilde{u}\tilde{w}}{\partial z}-\left[\frac{\partial \tilde{\tau}_{xx}}{\partial x}+\frac{\partial \tilde{\tau}_{xy}}{\partial y}+\frac{\partial \tilde{\tau}_{xz}}{\partial z}\right]+\left[\frac{\partial \sigma_{xx}}{\partial x}+\frac{\partial \sigma_{xy}}{\partial y}+\frac{\partial \sigma_{xz}}{\partial z}\right]=0 \tag{2}$$

$$\frac{\partial \bar{\rho}\tilde{v}}{\partial t}+\frac{\partial \bar{\rho}\tilde{u}\tilde{v}}{\partial x}+\frac{\partial\left(\bar{\rho}\tilde{v}^2+\bar{p}\right)}{\partial y}+\frac{\partial \bar{\rho}\tilde{v}\tilde{w}}{\partial z}-\left[\frac{\partial \tilde{\tau}_{xy}}{\partial x}+\frac{\partial \tilde{\tau}_{yy}}{\partial y}+\frac{\partial \tilde{\tau}_{yz}}{\partial z}\right]+\left[\frac{\partial \sigma_{xy}}{\partial x}+\frac{\partial \sigma_{yy}}{\partial y}+\frac{\partial \sigma_{yz}}{\partial z}\right]=0 \tag{3}$$

$$\frac{\partial \bar{\rho}\tilde{w}}{\partial t}+\frac{\partial \bar{\rho}\tilde{u}\tilde{w}}{\partial x}+\frac{\partial \bar{\rho}\tilde{v}\tilde{w}}{\partial y}+\frac{\partial\left(\bar{\rho}\tilde{w}^2+\bar{p}\right)}{\partial z}-\left[\frac{\partial \tilde{\tau}_{xz}}{\partial x}+\frac{\partial \tilde{\tau}_{yz}}{\partial y}+\frac{\partial \tilde{\tau}_{zz}}{\partial z}\right]+\left[\frac{\partial \sigma_{xz}}{\partial x}+\frac{\partial \sigma_{yz}}{\partial y}+\frac{\partial \sigma_{zz}}{\partial z}\right]=0 \tag{4}$$

where the viscous stress tensor τ_{ij} $(i,j=1, 2, 3)$ is:

$$\tilde{\tau}_{ij}=\mu\left[\left(\frac{\partial \tilde{u}_i}{\partial x_j}+\frac{\partial \tilde{u}_j}{\partial x_i}\right)-\frac{2}{3}\delta_{ij}\frac{\partial \tilde{u}_k}{\partial x_k}\right] \tag{5}$$

The bar in the LES equations denotes a filtered or large-scale flow quantity, defined as

$$\bar{f}=\int_D G(\vec{x}-\vec{x}')\,f(\vec{x}')d\vec{x}' \tag{6}$$

where G is a spatial filter and the integral is over the flow domain, D. The tilde in the LES equations denotes a Favre-filtered (density-weighted) variable, defined as

$$\tilde{f}=\frac{\overline{\rho f}}{\bar{\rho}} \tag{7}$$

The LES equations are essentially the continuity and momentum equations written for the filtered variables plus the additional subgrid terms, Eq. (8), in the momentum equations. In Bui (2000), for low-Mach numbers, these terms are approximated using Eq. (9).

$$\sigma_{kl}=\bar{\rho}(\widetilde{u_k u_l}-\tilde{u}_k\tilde{u}_l) \tag{8}$$

$$\sigma_{kl}=-\bar{\rho}C_s\Delta^2\left|\tilde{S}\right|\left(2\tilde{S}_{kl}-\frac{2}{3}\tilde{S}_{jj}\delta_{kl}\right) \tag{9}$$

The filtered velocity gradient tensor is

$$\tilde{S}_{kl}=\frac{1}{2}\left(\frac{\partial \tilde{u}_k}{\partial x_i}+\frac{\partial \tilde{u}_l}{\partial x_k}\right) \tag{10}$$

and

$$\left|\tilde{S}\right|=\left(2\tilde{S}_{kl}\tilde{S}_{kl}\right)^{1/2} \tag{11}$$

$$C_s=C_{so}^2\left[1-\exp\left(-c^+/25\right)^3\right] \tag{12}$$

where c^+ is the normal distance from the wall, defined as

$$c^+=\frac{\rho u_\tau c}{\mu} \tag{13}$$

In Eq. (12), the Smagorinsky constant *Cso*=0.15 is multiplied by the Van Driest damping function to account for the wall viscous sublayer.

The LES continuity equation and the definition of isothermal compressibility - Anderson (1990) are shown in Eqs. (14) and (15), respectively.

$$\frac{\partial \bar{\rho}}{\partial t} + \nabla \cdot \left(\bar{\rho} \tilde{\vec{V}} \right) = 0 \tag{14}$$

$$\tau = \left. \frac{1}{\rho} \frac{\partial \rho}{\partial p} \right)_T \tag{15}$$

According to Wanderley (2001), a Taylor's series expansion of the density with respect to pressure around p_∞ is obtained, as in Eq. (16). Here, only isothermal flows are considered.

$$\bar{\rho} = \rho_\infty + \left. \frac{\partial \bar{\rho}}{\partial \bar{p}} \right)_\infty (\bar{p} - p_\infty) + \frac{1}{2} \left. \frac{\partial^2 \bar{\rho}}{\partial \bar{p}^2} \right)_\infty (\bar{p} - p_\infty)^2 + \cdots \tag{16}$$

Combining the definition of isothermal compressibility given in Eq. (15) and the Taylor's series expansion given in Eq. (16), a relation between the density and the pressure is obtained where the isothermal compressibility appears as coefficient, Eq. (17).

$$\bar{\rho} = \rho_\infty + \rho_\infty \tau (\bar{p} - p_\infty) + \frac{1}{2} \rho_\infty \tau^2 (\bar{p} - p_\infty)^2 + \cdots \tag{17}$$

Since τ is very small, it is enough to consider only the first two terms of expansion (17) to express the density in terms of the pressure. After rearranging the resulting expression, Eq. (18) is obtained.

$$\bar{\rho} = \rho_\infty (1 - \tau p_\infty) + \rho_\infty \tau \bar{p} \tag{18}$$

Substituting Eq. (18) into Eq. (14), results Eq. (19).

$$\tau \rho_\infty \left[\frac{\partial \bar{p}}{\partial t} + \nabla \cdot \left(\bar{p} \tilde{\vec{V}} \right) \right] + \rho_\infty (1 - \tau p_\infty) \nabla \cdot \tilde{\vec{V}} = 0 \tag{19}$$

In the incompressible formulation, where is assumed that $\tau=0$, Eq. (19) reduces to Eq. (20).

$$\nabla \cdot \tilde{\vec{V}} = 0 \tag{20}$$

However, Eq. (20) is very difficult to solve numerically due to the absence of any term of time derivative. Fortunately, a more convenient equation can be obtained if the compressibility of the fluids is considered and a convenient value for the reference pressure p_∞ is assumed. Observed that Eq. (19) is satisfied also when

$$p_\infty = \frac{1}{\tau} \tag{21}$$

and

$$\frac{\partial \bar{p}}{\partial t} + \nabla \cdot \left(\bar{p} \tilde{\vec{V}} \right) = 0 \tag{22}$$

Therefore, the continuity equation given in Eq. (14) reduces to Eq. (22) with the condition given in Eq. (21). Observe that Eq. (22) is much easier to solve numerically than Eq.(20) due to the term of time derivative of the pressure that appears in the former equation. Let's considerer now the momentum equations given in Eqs. (2), (3), and (4). The substitution of Eq. (18) into the momentum equations will bring an unnecessary complexity to the problem without any improvement in precision, since the isothermal compressibility is very small. On the other hand, the substitution of $\rho=\rho_\infty$ introduces a convenient simplification of the problem without any degeneration of the momentum equations. After substituting $\rho=\rho_\infty$ into the momentum equations, Eqs. (23), (24), and (25) are obtained.

$$\frac{\partial \tilde{u}}{\partial t}+\frac{\partial\left(\tilde{u}^2+\bar{p}/\rho_\infty\right)}{\partial x}+\frac{\partial \tilde{u}\tilde{v}}{\partial y}+\frac{\partial \tilde{u}\tilde{w}}{\partial z}-\frac{1}{\rho_\infty}\left[\frac{\partial \tilde{\tau}_{xx}}{\partial x}+\frac{\partial \tilde{\tau}_{xy}}{\partial y}+\frac{\partial \tilde{\tau}_{xz}}{\partial z}\right]+\frac{1}{\rho_\infty}\left[\frac{\partial \sigma_{xx}}{\partial x}+\frac{\partial \sigma_{xy}}{\partial y}+\frac{\partial \sigma_{xz}}{\partial z}\right]=0 \tag{23}$$

$$\frac{\partial \tilde{v}}{\partial t}+\frac{\partial \tilde{u}\tilde{v}}{\partial x}+\frac{\partial\left(\tilde{v}^2+\bar{p}/\rho_\infty\right)}{\partial y}+\frac{\partial \tilde{v}\tilde{w}}{\partial z}-\frac{1}{\rho_\infty}\left[\frac{\partial \tilde{\tau}_{xy}}{\partial x}+\frac{\partial \tilde{\tau}_{yy}}{\partial y}+\frac{\partial \tilde{\tau}_{yz}}{\partial z}\right]+\frac{1}{\rho_\infty}\left[\frac{\partial \sigma_{xy}}{\partial x}+\frac{\partial \sigma_{yy}}{\partial y}+\frac{\partial \sigma_{yz}}{\partial z}\right]=0 \tag{24}$$

$$\frac{\partial \tilde{w}}{\partial t}+\frac{\partial \tilde{u}\tilde{w}}{\partial x}+\frac{\partial \tilde{v}\tilde{w}}{\partial y}+\frac{\partial\left(\tilde{w}^2+\bar{p}/\rho_\infty\right)}{\partial z}-\frac{1}{\rho_\infty}\left[\frac{\partial \tilde{\tau}_{xz}}{\partial x}+\frac{\partial \tilde{\tau}_{yz}}{\partial y}+\frac{\partial \tilde{\tau}_{zz}}{\partial z}\right]+\frac{1}{\rho_\infty}\left[\frac{\partial \sigma_{xz}}{\partial x}+\frac{\partial \sigma_{yz}}{\partial y}+\frac{\partial \sigma_{zz}}{\partial z}\right]=0 \tag{25}$$

Equations (22) through (25) are very convenient for numerical solution because all of them have a time derivative term that facilitates substantially the implementation of any method of time integration. To solve the problem of the flow around a circular cylinder, it is convenient to write Eqs. (22) through (25) in general 2-D curvilinear coordinates, in the conservative form, and in the dimensionless form, see Eq. (26):

$$Q_t+\left(E_e-E_v\right)_\xi+\left(F_e-F_v\right)_\eta=0 \tag{26}$$

where

$$Q=\frac{1}{J}\begin{Bmatrix} p \\ u \\ v \end{Bmatrix}, \qquad E_e=\frac{1}{J}\begin{Bmatrix} pU \\ uU+p\xi_x \\ vU+p\xi_y \end{Bmatrix}, \quad F_e=\frac{1}{J}\begin{Bmatrix} pV \\ uV+p\eta_x \\ vV+p\eta_y \end{Bmatrix} \tag{27}$$

$$E_v=\frac{(1+\mu_{sgs})}{J\,\mathrm{Re}}\begin{Bmatrix} 0 \\ A_1u_\xi+A_2u_\eta+A_3v_\xi+A_4v_\eta \\ A_3u_\xi+A_5u_\eta+A_6v_\xi+A_7v_\eta \end{Bmatrix}, F_v=\frac{(1+\mu_{sgs})}{J\,\mathrm{Re}}\begin{Bmatrix} 0 \\ A_2u_\xi+A_{10}u_\eta+A_5v_\xi+A_{11}v_\eta \\ A_4u_\xi+A_{11}u_\eta+A_7v_\xi+A_{12}v_\eta \end{Bmatrix} \tag{28}$$

$$\begin{aligned} &\mu_{sgs}=R_eC_s^2\Delta^2\left|\bar{S}\right|, \quad a_\infty=\sqrt{\frac{1}{\rho_\infty\tau}}, \quad \mathrm{Re}=\frac{\rho_\infty U_\infty d}{\mu_\infty}, \quad M_\infty=\frac{U_\infty}{a_\infty} \\ &U=\xi_t+u\xi_x+v\xi_y \\ &V=\eta_t+u\eta_x+v\eta_y \\ &J=\xi_x\eta_y-\eta_x\xi_y \end{aligned} \tag{29}$$

where A_1, A_2, A_3, etc. are related to the metrics of the transformation.

Equation (26) is solved numerically together with the initial conditions, boundary conditions on the body surface, and free-stream boundary conditions given in Eqs. (30), respectively:

$$\begin{cases} u=1 \\ v=0 \\ p=1/M_\infty^2 \end{cases}, \quad \begin{cases} u=\dot{y} \\ v=0 \\ \dfrac{\partial p}{\partial \eta}=0 \end{cases}, \quad \begin{cases} u=1 \\ v=0 \\ p=1/M_\infty^2 \end{cases}, \qquad M_\infty=0.2 \tag{30}$$

The equation of motion of the body is obtained by applying the second Newton's law to a cylinder of mass (m) subjected to lift (L), spring (k), and damping (ζ) forces. The dimensionless form of the equation of motion (31) with the

initial conditions (32) is solved simultaneously with the Navier-Stokes equations to compute the velocity $(\dot{y})$ (it is also necessary to impose the no-slip condition on the body), and the position (y) of the cylinder (to place the body at its new position to regenerate the grid).

$$\ddot{y} + C_\zeta \dot{y} + C_k y = \frac{C_L(R_e)}{2C_\mu} \tag{31}$$

$$y(0) = 0 \quad , \quad \dot{y}(0) = 0 \tag{32}$$

where

$$C_\mu = \frac{m}{\rho D^2} \quad , \quad C_k = \frac{4\pi^2}{U_r^2} \quad , \quad C_\zeta = \frac{4\pi\zeta}{U_r} \quad , \quad U_r = \frac{U}{f_n d} \tag{33}$$

3. Numerical Formulation

Central difference schemes require artificial dissipation to improve stability – Pulliam (1986). The artificial dissipation suppresses high frequency oscillations and controls the odd-even uncoupling inherent to central difference schemes. The Von-Neumann linear stability analysis applied to the Beam-Warming central difference scheme shows that some artificial dissipation is required to improve stability. This can be accomplished by adding a fourth-order explicit dissipation term to the right-hand side and a second-order implicit smoothing term to the left-hand side, as shown in Eq. (34).

$$\begin{aligned} &\left(I + \Delta t \delta_\xi A^n - \Delta t \nabla_\xi M_\xi^n \Delta_\xi J + D_\xi^{(2)}\right) f^n = -\Delta t \left(\delta_\xi E + \delta_\eta F\right)^n + D^{(4)} \\ &\left(I + \Delta t \delta_\eta B^n - \Delta t \nabla_\eta M_\eta^n \Delta_\eta J + D_\eta^{(2)}\right) \Delta Q^n = f^n \end{aligned} \tag{34}$$

where

$$\begin{aligned} &A^n = \left.\frac{\partial E_e}{\partial Q}\right)^n, \quad B^n = \left.\frac{\partial F_e}{\partial Q}\right)^n \\ &M_\xi^n = \left.\frac{\partial E_v}{\partial \overline{Q}_\xi}\right)^n, \quad M_\eta^n = \left.\frac{\partial F_v}{\partial \overline{Q}_\eta}\right)^n \end{aligned} , \quad \begin{aligned} &E^n = E_e^n - E_v^n \qquad D_\xi^{(2)} = -\varepsilon_i \Delta t J^{-1} \nabla_\xi \Delta_\xi J \\ &F^n = F_e^n - F_v^n \quad , D_\eta^{(2)} = -\varepsilon_i \Delta t J^{-1} \nabla_\eta \Delta_\eta J \\ &\overline{Q} = JQ \qquad D^{(4)} = -\varepsilon_e \Delta t J^{-1} \left[\left(\nabla_\xi \Delta_\xi\right)^2 + \left(\nabla_\eta \Delta_\eta\right)^2\right] J Q^n \end{aligned} \tag{35}$$

The numerical solution of the flow around a vibrating circular cylinder requires the specification of boundary conditions at the boundaries of the physical domain. The no-slip condition is imposed on the body surface and the free-stream condition at the external boundary. At the outflow boundary, extrapolation of order zero is used to evaluate the properties of the flow at that boundary. To eliminate reflections, a buffer-zone is specified where disturbances are damped away by a weighting function S, according to Eq. (36). The weighting function gradually suppresses the disturbances up to zero at the outflow boundary.

$$\begin{aligned} p_{i,j} &= p_\infty + (p_{i,j} - p_\infty) S_j \\ u_{i,j} &= u_\infty + (u_{i,j} - u_\infty) S_j \\ v_{i,j} &= v_\infty + (v_{i,j} - v_\infty) S_j \end{aligned} \qquad S_j = \left(\frac{1 + \tanh(\arg)}{2}\right), \qquad \arg = 4\left\{1 - \frac{2(j - j_{buf})}{(j_{\max} - j_{buf})}\right\} \tag{36}$$

An algebraic grid generator using the multi-surface method – Fletcher (1988) - is used to generate grid points around a circular cylinder. The grid is constructed such that the body is part of the grid (body fitted grid). In addition, the generated grid is locally orthogonal to the body surface to facilitate the implementation of the boundary condition on the body. In order to concentrate grid points next to the nose and body surface, an exponential stretching is used in both stream-wise (ξ) and transversal (η) directions.

The equation of motion is solved simultaneously with the Navier-Stokes equations to compute the velocity $\dot{y}$ and position y of the cylinder. These are necessary to impose the no-slip condition on the body surface and to positioning the body to generate the new grid points. The Lax-Wendroff method (37) and Euler explicit method (38) were used to compute the position and velocity of the cylinder, respectively. In Eq. (39), the lift coefficient C_L is obtained from the integration of the pressure and skin friction distribution around the cylinder surface obtained from the Navier-Stokes previous iteration.

$$y^{n+1} = y^n + \dot{y}^n \Delta t + \frac{1}{2}\ddot{y}^n \Delta t^2 \tag{37}$$

$$\dot{y}^{n+1} = \dot{y}^n + \ddot{y}^n \Delta t \tag{38}$$

where

$$\ddot{y}^n = \frac{C_L^n}{2C_\mu} - C_\zeta \dot{y}^n - C_k y^n \tag{39}$$

4. Fixed Cilinder

Results for *Re*=40, 100, and 200 are compared with other numerical and experimental data to check the accuracy of the obtained results. An O-grid was generated around a fixed circular cylinder with 120x120 nodes, using stretching parameter q_η=1.025 in the radial direction. The distance between the body surface and the external boundary equal to 20 diameters proved to be enough, see Fig. 1.

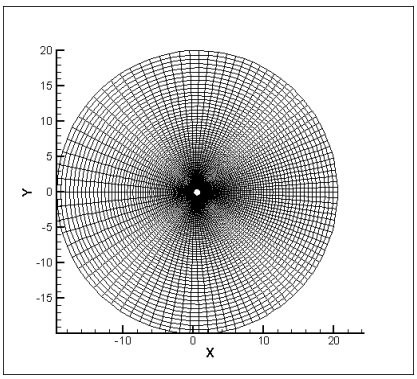

Figure 1. Computational Grid in the Physical Domain

Figure 2a shows comparisons between the pressure distribution obtained in the present work and other numerical and experimental data obtained from the literature for *Re*=40. The agreement is quite remarkable. Figure 2b shows the pressure field and streamlines around a circular cylinder for *Re*=40. The pressure map shows the stagnation point in violet at the leading edge of the cylinder and the low pressure in blue at the top and bottom of the cylinder. The streamlines show the two vortices attached at the trailing edge of the cylinder due to the separation of the boundary layer.

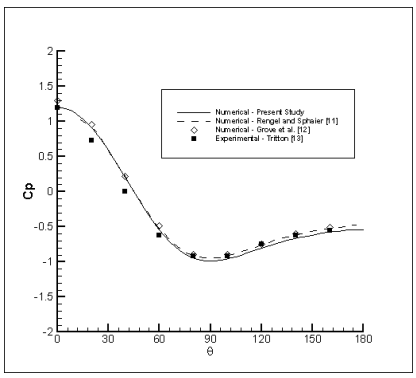

(a)

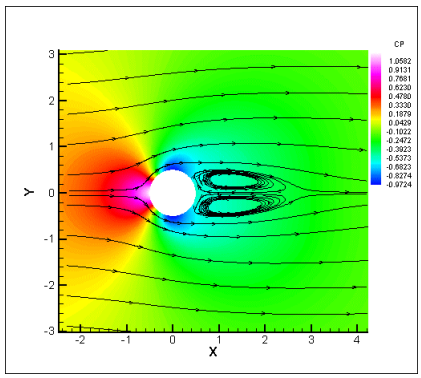

(b)

Figure 2. Pressure Distribution around a Circular Cylinder for *Re*=40 (a) pressure distribution on the body surface and (b) pressure map and stream lines around the cylinder..

Table 2 shows results obtained for *Re*=40 for the drag coefficient. The agreement between the results obtained in the present work and other numerical and experimental data is again remarkable. Moreover, the convergence time required by the Beam and Warming scheme to solve the present governing equations is substantial and unprecedently low if one considers the type of computer used in the present calculation.

Table 2. Comparison Between Results Obtained by the Present Work and other Numerical and Experimental Data.

Reference	*Re*	C_D	C_L	S_t	Observation
Triton Exp. (1959)	40	1.57	0.0	0.0	
Herfjord (1995)	100 200	1.36 1.35	0.34 0.70	0.168 0.196	Finite Elements N^0 of nodes, dt 10080, 0.002 10080, 0.005 10080, 0.0025
Rengel Sphaier (1999)	40 100 200	1.61 1.36 1.35	0.00 0.32 0.67	0.00 0.173 0.203	Finite Volume (180x160) Projection Method
Presente Study	**40** **100** **200**	**1.575** **1.358** **1.361**	**0.000** **0.313** **0.657**	**0.000** **0.161** **0.194**	**Finite Difference (120X120)**

Table 2 compares also results obtained by the present work and other acceptable numerical data for Strouhal number, drag, and lift coefficients at *Re*= 100 and 200. The agreement is considered good and demonstrates the quality of the results obtained by the present formulation.

Figure 4 shows the variation of the lift and drag coefficients as a function of time and Fig 5 shows the pressure map and stream lines for *Re*=100, and 200. It may be observed that the adopted governing equations are able to represent correctly the expected physics of the flow. For example, for *Re*=40, the lift coefficient is constant and equal to zero and the drag coefficient goes asymptotically to the correct value. For *Re*=100, and 200 oscillations take place for both the lift and drag coefficients. These oscillations are caused by the asymmetric pressure distribution on the body surface due to the vortex shedding known as Kármán vortex street.

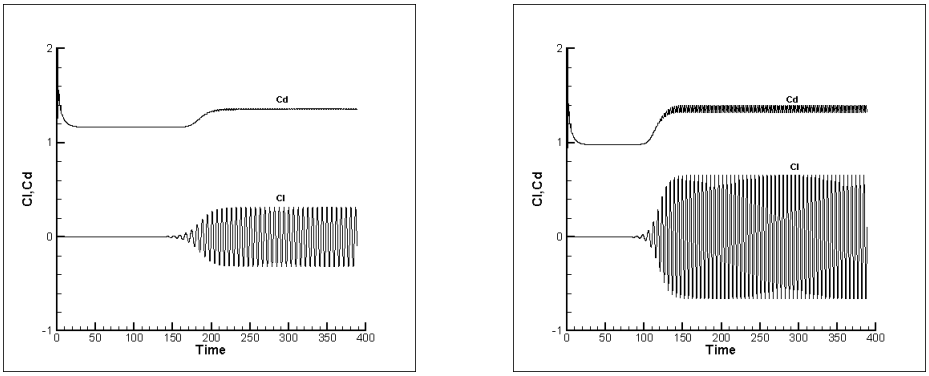

(a) (b)

Figure 4. Time Variation of Lift and Drag Coefficients of a Cylinder, *Re* =100 (a); 200 (b).

In Figures 5, the low-pressure core that becomes stronger as the Reynolds number increases may identify the vortices that are transported by the mean flow. It is interesting to point out the oscillating pattern of the streamlines in the wake of the cylinder caused by the presence of the vortices. In addition, the streamlines oscillate at the same frequency as the vortex shedding.

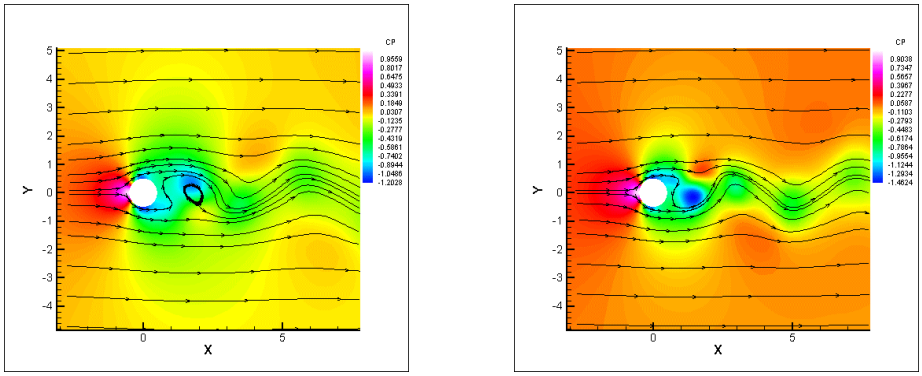

(a) (b)

Figure 5. Pressure Field and Streamlines Around a Circular Cylinder for *Re*=100 (a); 200 (b).

5. Moving Cylinder

Figure 6a shows the physical situation of interest. A circular cylinder of mass *m* subjected to an incident uniform flow, and supported by a spring and a dumper. The same mass and dumper coefficients used in Khalak and Williamson (1996) were used in the present investigation. These are C_μ=1.88 and C_ζ=5.42x10^{-3}, with the reduced velocity varying from 2 to 12 proportionally to the variation of the Reynolds number from 2000 to 12000.

An O-grid is generated (in each iteration) around a vibrating circular cylinder with 120x200 nodes, using stretching parameter q_η=1.025 in the radial direction. The distance between the body surface and the external boundary equal to 60 diameters proved to be enough.

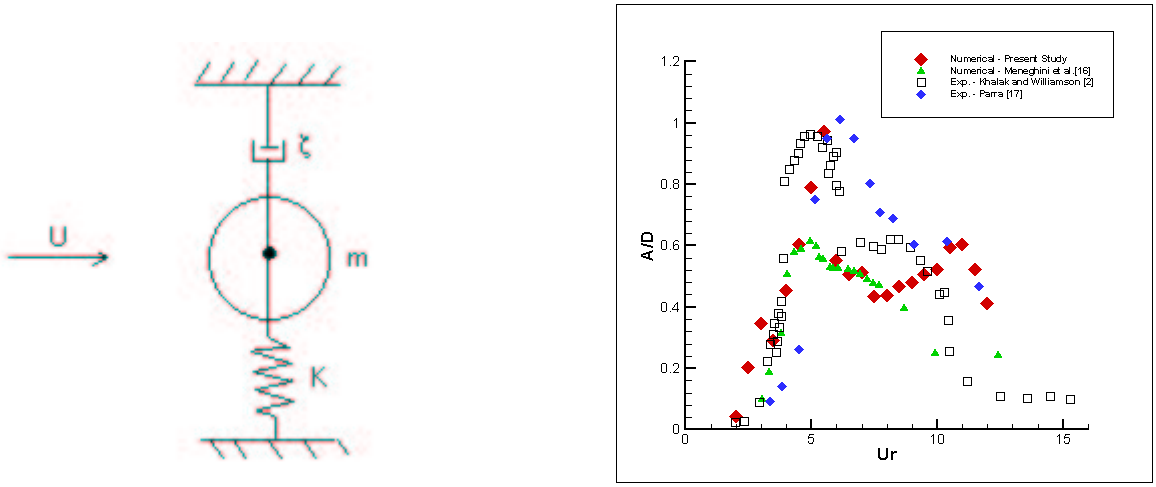

(a) (b)

Figure 6. (a) An Illustration of the Physical Situation of Interest and (b) the Amplitude of Oscillation as a Function of Reduced Velocity

Figure 6b shows the amplitude of oscillation as a function of the reduced velocity obtained in the present work and other numerical and experimental data from the literature for comparison. Figure 6b shows that our mathematical and numerical formulations were able to capture the upper and lower branch reported in Khalak and Williamson (1996) (shown in Fig. 6b as red diamonds). Moreover, the numerical results obtained are much closer to the experimental data than other numerical results.

Figures 8a,b show results obtained for the transversal displacement of the vibrating circular cylinder as a function of time. It is considered the time trace in two regions: in the build-up of the upper branch and at the top of the upper branch. The reduced velocities of U_r=4.5 in Fig. 8a and U_r=6.0 in Fig. 8b correspond to the build-up and top of the upper branch, respectively. The displacement agree well qualitatively with those data from Khalak and Williamson (1996) regarding the observed combination of frequencies.

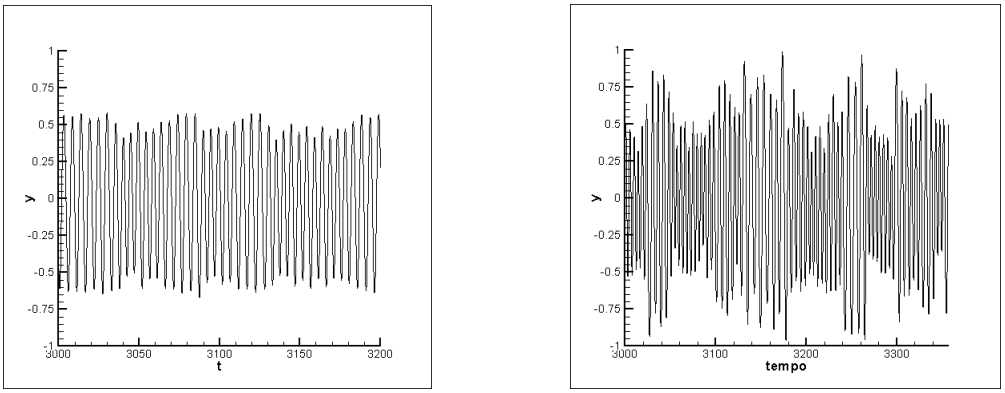

(a) (b)

Figure 8. Transversal Displacement of the Circular Cylinder for (a) U_r=4.5 and (b) U_r=5.5.

Figures 9a,b show results obtained for the transversal displacement of the vibrating circular cylinder as a function of time. It is considered the time trace in two regions: in the lower branch and in the declining region away from the lower branch. The reduced velocities of U_r=8.0 in Fig. 9a and U_r=12.0 in Fig. 9b correspond to the lower branch and the declining region away from the lower branch, respectively. According to Khalak and Williamson (1996), the response in the lower branch is very periodic and looks like a pure single frequency. In Fig. 9a of the present work, it is not observed a single frequency, but a combination of frequencies. On the other hand, Fig. 9b seems to agree qualitatively with the experimental data regarding the no uniform amplitude and the overall lower response.

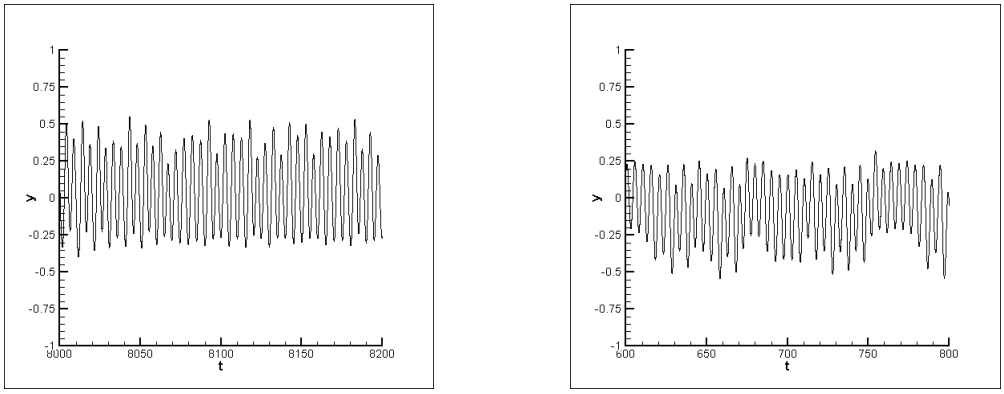

(a) (b)

Figure 9. Transversal Displacement of the Circular Cylinder for (a) U_r=8.0 and (b) U_r=12.0.

6. Conclusions

The motivation for the present work was to duplicate through numerical simulation the experimental results obtained by Khalak and Williamson (1996) for the vortex-induced vibrations of a circular cylinder. To check the good quality and efficiency of the algorithm, results were obtained for the fixed cylinder and compared to other consecrated data before applying on the vibrating cylinder problem.

The results for the fixed cylinder agree very well with those obtained through other reliable methods for solving the incompressible Navier-Stokes equations. The time required for convergence using the Beam and Warming implicit scheme proved to be lower than other known methods for the solution of the incompressible Navier-Stokes equations. The numerical solution provided a good picture of the real physics of the phenomenon showing the Kármán vortex street oscillation of the lift and drag coefficients due to the asymmetric pressure distribution around the cylinder.

The results obtained for the vibrating cylinder agree very well with those experimental data obtained from the literature not only quantitatively, but also qualitatively in the upper branch. In the lower branch, the poor quantitative agreement seems to be related to the insufficient grid refinement for the higher Reynolds number of that flow regime. The present mathematical and numerical formulations were able to capture the upper and lower branch of the amplitudes of oscillation reported in Khalak and Williamson (1996). The variation of Reynolds number with the reduced velocity seems to have a significant effect on the amplitude of oscillation. Possible explanations for the good performance of the present formulation to simulate the VIV phenomenon are listed below:

- The governing equations are in the conservative form;
- The numerical efficiency of the algorithm permitted to obtain a wider number of cycles of oscillation in a permissible time of computation giving a much better view of the VIV phenomenon;
- The distance from the body surface to the external boundary of 60 diameters;
- The buffer zone extending from 30 to 60 diameters to eliminate possible reflections of perturbations in the external boundary that could effect the flow around the body;
- The variation of the Reynolds number with the reduced velocity to reproduce the real experimental procedure in Khalak and Williamson (1996);
- The use of a no dissipative scheme with the explicit addition of artificial dissipation allowing the control of the dissipation level.

Finite difference method can be a quite powerful tool to study vortex-induced vibration of offshore structures. It is a versatile method that allows an accurate and reliable identification of the flow characteristics around the body including the intensity, location and frequency of the vortex shedding in the wake necessary to investigate the induced vibration phenomenon. Further investigation will include the use of finer grid to improve the results in the lower branch, analysis of three-dimensional effects on the induced vibrations. Other applications that can be handled by the finite difference method may include the shadow effects, multi-body dynamics among other problems of interest in offshore engineering.

7. Acknowledgments

The authors would like to present their special thanks to the Brazilian Agency for Science and Technology Development - CNPq for the full financial support of the present research.

8. References

Anderson, D. A., Tannehill, J. C., and Pletcher, R. H., 1984, Computational Fluid Mechnics and Heat Transfer. McGraw-Hill, New York.

Anderson, J. D., 1990, Modern Compressible Flow: With Historical Perspective. McGraw-Hill, New York.

Beam, R. M., and Warming, R. F., 1978, "An Implicit Factored Scheme for the Compressible Navier-Stokes Equations," AIAA Journal, **16**, No. 4, pp. 393-402.

Bearman, P. W., 2000, "Developments in Vortex Shedding Research," Workshop on Vortex-Induced Vibrations of Offshore Structures. São Paulo, Brazil.

Bui, T. T., 2000, "A parallel Finite Volume Algorithm for Large Eddy Simulation of Turbulent Flows," International Journal of Computational Fluid Dynamics, **29**, pp. 877-915.

Constanceau, M., and Bouard, R., 1977, "Experimental Determination of the Main Features of Viscous Flow in the Wake of a Circular Cylinder in Uniform Translation Steady Flow," Journal of Fluid Mechanics, **79**, pp. 231-256.

Flatschart, R. B., Meneghini, J. R., and Saltara, F., 2000,"Large Eddy Simulation of the Flow around Tube Bundles at High Reynolds Number," Workshop on Vortex-Induced Vibrations of Offshore Structures. August 14-16, São Paulo, Brazil.

Fletcher, C. A. J., 1988, Computatinal Techniques for Fluid Dynamics. Springer-Verlag, Berlin, Germany.

Grove, A. S., Shair, S. H., and Peterson, E. E., 1964, "An Experimental Investigation of the Steady Separated Flow Past a Circular Cylinder," Journal of Fluid Mechanics, **19**, pp. 60-80.

Herfjord, K., 1995, "A Study of Two-dimensional Separated Flow by a Combination of the Finite Element Method and Navier-Stokes Equations," Dr. Eng. Theses, The Norwegian Institute of Technology, Trondheim, Norway.

Khalak, A., and Williamson, C. H. K., 1996, "Dynamics of a Hydroelastic Cylinder with Very Low Mass and Damping," Journal and Fluids and Structures, **10**, pp. 455-472.

Meneghini, J. R., Saltara, F., and Bearman, P. W., 1997, "Numerical Simulation of Vortex Shedding from an Oscillating Circular Cylinder. Computational Methods and Experimental Measurements," Computational Mechanics Publications. Southampton, UK, editors P. Anangnostopolos, G. M. Carlomagno & C. A. Brebbia, p.409-418.

Parra, P. H. C. C., 1996, "Modelo Semi-empirico para Vortex-Induced Vibrations: Análise Teórica e Experimental," Dissertação de Mestrado apresentada à Escola Politécnica da Universidade de São Paulo, São Paulo, Brazil.

Pulliam, T. H., 1986, "Artificial Dissipation Models for the Euler Equation," AIAA Journal, **24**, No. 12, pp. 1931-1940.

Rengel, J. E., and Sphaier, S. H., 1999, "A Projection Method for Unsteady Navier-Stokes Equation with Finite Volume Method and Collocated Grid," Hybrid Methods in Heat and Mass Transfer, **1**, no 4..

Smagorinsky, J., 1963, "General Circulation Experiments with the Primitive Equations," Monthly Weather Review, **91**, pp. 99-164.

Tritton, D. J., 1959, Journal of Fluid Mechanics, **6**, p. 547.

Wanderley, J. B. V., 2001, "An Algorithm for Slightly Compressible Flows," Proceedings of the 20th International Conference on Offshore Mechanics and Artic Engineering. June 3-8, Rio de Janeiro, Brazil.